Journal of Computational Physics 229 (2010) 5999–6014

Contents lists available at ScienceDirect

Journal of Computational Physics

journal homepage: www.elsevier.com/locate/jcp

A weighted-integral based scheme

Li-Jun Xuan *, Jie-Zhi Wu [1]

State Key Laboratory for Turbulence and Complex Systems, College of Engineering, Peking University, Beijing 100871, China

ARTICLE INFO

Article history:
Received 7 October 2009
Received in revised form 13 March 2010
Accepted 20 April 2010
Available online 24 April 2010

Keywords:
Weighted-integral based scheme
WENO interpolation
Hyperbolic systems
High-order accuracy

ABSTRACT

A weighted-integral based scheme (WIBS) and a weighted essentially non-oscillatory (WENO)-WIBS are constructed, where the integral of the unknown function with a set of linearly independent test functions are recorded on every cell. The time evolutions of these recordings are computed with TVD Runge–Kutta method. At the boundary of every two cells, the function values are interpolated from the recordings of the neighboring cells to calculate flux and volumetric integral in the weak form.

Our basic idea is to increase the order of interpolation by increasing both the interpolating cells and cell recordings simultaneously. The interpolation on more cells naturally permits the use of WENO idea to capture the discontinuity, while more cell recordings can shrink the size of the interpolating stencil. The compactness of the reconstruction stencil can increase the accuracy and fully retain it at the boundary. The WIBS so constructed may include as special cases a quite general class of the numerical methods in computational fluid dynamics, such as finite-volume method, finite difference method, discontinuous Galerkin scheme, spectral volume method, spectral difference method, finite element method, and PnPm scheme recently designed by Dumbser et al. [Journal of Computational Physics 227 (2008) 8209–8253], etc.

In this paper the property of WIBS and WENO-WIBS on one-dimensional hyperbolic conservation-law systems is systematically explored. In addition to the high stability and order of accuracy for smooth region, the WENO-WIBS exhibits high resolution and non-oscillatory property in capturing the discontinuity. The numerical experiments of WIBS and WENO-WIBS on various benchmark problems are favorably compared with the results obtained by other high-order methods.

1. Introduction

High-order computational methods are extensively needed for solving problems in computational fluid dynamics (CFD). For flow problems with complex structures and broad range of characteristic scales, high resolution is necessary to extract correctly the information of the flow field. Examples include the direct numerical simulation (DNS) and the large-eddy simulation (LES) of turbulence, as well as computational aero-acoustics (CAA). Moreover, if the flow fields involve shock waves, those schemes should be non-oscillatory near discontinuities but without excessive damping of the turbulent or acoustic fluctuations.

Weighted essentially non-oscillatory (WENO) schemes ([11,8,2]) are a powerful class of high-order numerical schemes. It is very robust—having very good convergence properties and computational efficiency. Through weighted combination of the interpolations on sub-stencils (to select smooth sub-stencil near discontinuity and recover the high-order basic stencil

* Corresponding author.
E-mail address: ljxuanstar@gmail.com (L.-J. Xuan).
[1] Also at University of Tennessee Space Institute Tullahoma, TN 37388, USA.

0021-9991/$ - see front matter © 2010 Elsevier Inc. All rights reserved.
doi:10.1016/j.jcp.2010.04.031

interpolation in smooth region), the numerical oscillations near the discontinuities are effectively suppressed and, at the same time, the high accuracy order is successfully achieved in smooth region. But numerical tests indicate that classical WENO schemes are usually not optimal for computing turbulent flows or aero-acoustic fields because they may lead to a significant damping of the turbulent or acoustic fluctuations, i.e. they are too diffusive for short waves.

In compact scheme [10] and discontinuous Galerkin scheme (DG) [20], there are more than one recordings on every cell, by which the size of interpolation stencil is greatly shrunk, resulting in a high resolution for short waves in smooth region. But, as is well known, compact scheme is hard to be extended to unstructured meshes and not suitable for capturing discontinuities, because the excessive recordings are not locally updated. While in DG the numerical oscillations is suppressed by flux limiter, which often leads to deterioration of accuracy near the extrema in smooth region.

How to incorporate compact stencil and WENO interpolation into one scheme has been the goal of many recent efforts. These include the hybrid compact-ENO/WENO scheme ([1,12,9,14]), where in the smooth region a compact scheme is used, while in the region near discontinuities a scheme that can capture discontinuity without oscillation is used. However, although this hybrid approach does overcome some drawbacks of both compact and WENO schemes, new problems could arise. For example, indicators are needed to distinguish discontinuities, and switching between the two schemes may cause a loss in accuracy. Moreover, since the two schemes have different structures, the hybrid scheme is often inefficient in parallel computing. A recent development in this area can be found in Zhang's paper [21], where the related information are also introduced.

Another attempt is Hermite WENO scheme, where not only the primitive variable but also its derivatives are evolved in time. For this purpose, a Hermite polynomial is defined to interpolate the solution and its derivatives. Van-Leer [19] was the first to study in detail such schemes in a finite-difference context, which was followed by many studies such as Refs. [6,3,13]. Recently, Qiu and Shu [15,16] proposed a 5th-order WENO scheme based on Hermite polynomials for solving 1D nonlinear conservation-law systems. Later, Capdeville [4] has made more exploration, including the new weighted combination methods and many other problems.

Based on the frame of DG, many improvements have been explored to incorporate WENO interpolation to save memory cost and increase the stability. For example Balsara et al. [23] have developed a kind of hybrid RKDG-HWENO scheme where a WENO construction is designed to recover the higher moments in DG method. They used limiter to capture discontinuities in troublesome zones. More recently, Dumbser et al. [7] have developed a kind of PnPm scheme, where, on every cell, orthogonal bases are used and the order of accuracy is increased by using the information not only on every cell but also on its neighboring cells to interpolate the function valve. The general frame of this scheme is the Galerkin method. On every cell the differential equation is locally solved and a Riemann solver is used to compute the boundary flux, by which the order of accuracy in time direction can reach the same order as that of spatial one. This method can increase the order of accuracy by adding the cell recordings and interpolating cells at the same time, which makes it easy to construct very high order scheme.

Further investigations have shown that the stability of PnPm is better than the original DG scheme. Dumbser et al. [7] have also tried to incorporate WENO method in the interpolation step to capture discontinuity. They showed some experiments on the case, where there is only one recording on every cell (corresponding to finite-volume method), and mentioned that the WENO procedure for the case of more than one-cell recordings was still under exploring.

In this paper, we follow Dumbser et al.'s [7] concept to add cell recordings and interpolating cells at the same time, but construct our scheme in a framework different from the Galerkin method, which is more general and fundamental: the weighted-integral of the equation on every cell. In other words, it is a weighted-integral based scheme (WIBS). The cell recordings are chosen to be the weighted integration of the unknown function with a set of linearly independent (not necessarily orthogonal) test functions, which are easier to construct compared to the PnPm scheme, where the test functions must be orthogonal. In our scheme, the function value is interpolated on every half cell (not the full cell) region and a TVD Runge–Kutta method [17] is used in temporal integration. As to the capture of discontinuities, we add the WENO interpolation into WIBS (WENO-WIBS) for the case of two-cell recordings. Because positive optimal weights do not always exist in Hermite interpolation, we constructed a new weighed combination with no use of the optimal weights.

The WIBS so constructed may include a quite general class of the numerical methods in computational fluid dynamics as special cases. A proper choice of the test functions and interpolation method in WIBS can recover many existing methods, such as finite difference method, finite volume method, DG, spectral volume method [20], spectral difference method [20], finite element method, and PnPm [7], etc.

This paper explores the property of WIBS and WENO-WIBS on 1-dimensional (1D) hyperbolic conservation-law equation. On various benchmark problems, WIBS and WENO-WIBS show their strong stability, high-order of accuracy, and high resolution for short waves. A high resolution for discontinuities is also found with very small numerical oscillation.

Compared to RKDG-HWENO [23] and PnPm [7] schemes, the WIBS and WENO-WIBS have several advantages and differences:

1. Because WIBS is based on the weak form (not Galerkin method), the test functions of WIBS are not necessarily orthogonal and so easier to construct. The only restriction is their linear independence.
2. WIBS is more stable than PnPm.
3. WENO-WIBS has better effects on capturing discontinuity than PnPm.
4. Our WENO procedure does not need the existence of positive optimal weights, which is different from RKDG-HWENO and many other WENO methods.

In Section 2 we present the construction of WIBS of various orders and an analytical discussion of the stability of 3rd-order WIBS. The construction of WENO-WIBS is introduced in Section 3. In Section 4 the schemes are numerically tested regarding to their stability, accuracy, resolution on short waves, and discontinuity capturing. Conclusion remarks are given in Section 5.

2. The construction of WIBS

Consider one-dimensional (1D) scalar conservative law

$$u_t + f(u)_x = 0. \tag{1}$$

For simplicity, assume the grid points $\{x_{i-1/2}\}$ are uniformly distributed with the cell size $x_{i+1/2} - x_{i-1/2} = \Delta x$ and cell centers $x_i = \frac{1}{2}(x_{i+1/2} + x_{i-1/2})$. Denote the cells by $I_i = [x_{i-1/2}, x_{i+1/2}]$.

On every cell we record the integrals:

$$v_{im} = \int_{I_i} u(x)\phi_{im}(x)dx \equiv \langle u, \phi_{im}\rangle_{I_i}, \tag{2}$$

where $\{\phi_{im}(x)\}_{m=1,\ldots,M}$ is a set of linearly independent test functions and the notation $\langle\cdot\rangle_{I_i}$ means integral over I_i. Integrating (1) $\times\ \phi_{im}(x)$ over I_i, we obtain a weak form of the conservation law:

$$\frac{dv_{im}}{dt} + f(u)\phi_{im}|_{\partial I_i} - \langle f(u), \partial_x\phi_{im}\rangle_{I_i} = 0. \tag{3}$$

For very half cell $x \in [x_i, x_{i+1}]$, function $u(x)$ can be interpolated by the neighboring cell recordings $v_{jm}(j = i + K_1, i + K_1 + 1, \ldots, i + K_2, m \in [0, M], K_1, K_2 \in \mathbb{Z}, K_1 \leqslant K_2)$. With this approximate $u(x)$ we can calculate the function values at $x_{i+1/2}$ and $x_{i+\alpha_l}(\alpha_l \in (0,1), l = 1, 2, \ldots, L)$, where L depends on the order of the scheme. The numerical flux at these points, denoted by $\hat{f}_{i+1/2}$ and $\hat{f}_{i+\alpha_l}$, can be obtained:

$$\hat{f}_{i+1/2} = h(u^-_{i+1/2}, u^+_{i+1/2}), \quad \hat{f}_{i+\alpha_l} = h(u^-_{i+\alpha_l}, u^+_{i+\alpha_l}), \tag{4}$$

where u^- and u^+ are numerical approximations to the point values from left and right, respectively. The fluxes in (4) satisfy the usual numerical fluxes conditions such as Lipschitz continuity and consistency, etc. In this paper we choose the following local Lax–Friedrichs flux:

$$h(a,b) = \frac{1}{2}[f(a) + f(b) + c(a-b)], \tag{5}$$

where $c = \max_{u\in D}|f'(u)|$, $D = [\min(a,b), \max(a,b)]$.

The second term $f(u)\phi_{im}|_{\partial I_i}$ in (3) can be computed from half-point numerical flux $\hat{f}_{i+1/2}$. As to the third term, with $\hat{f}_{i-1+\alpha_l}, \hat{f}_{i-1/2}$ and $\hat{f}_{i+\alpha_l}, \hat{f}_{i+1/2}$, the function $f(u)$ can be interpolated to calculate the integral. The method of lines ODEs are then integrated by a TVD Runge–Kutta method in [17], of which the third-order version is used in the present paper. This is the whole construction of the scheme.

It is easily found that if $\{\phi_{im}\}$ and the reconstruction method of $u(x)$ are properly chosen, almost all of the existing schemes can be recovered from the present framework. For example, setting $\{\phi_{im}\} = 1$ would recover the classical finite-volume method. If $\{\phi_{im}\} = \delta(x)$ and the reconstruction is targeted to approximating the derivatives, the scheme would become the classical finite difference method. As $\{\phi_{im}\}$ is chosen as a set of independent functions, if the boundary and volumetric integrals are obtained in the same way as those in DG method, the scheme would recover or become equivalent to DG. Moreover, if

$$\phi_{im} = 1 \quad \forall x \in I_{im}, \qquad \phi_{im} = 0 \quad \forall x \notin I_{im}, \tag{6}$$

where $I_{im} \subset I_i, I_{im} \cap I_{in} = \varnothing (m \neq n), \bigcup_m I_{im} = I_i$, and a corresponding reconstruction of $u(x)$ and the numerical fluxes are used, we would obtain spectral volume method [20]. It is also easy to recover spectral difference method, finite element method, and many other existing methods, which will not be shown here one by one.

In the following subsections A to E, we give the details of a class of 2nd- to 10th-order schemes for 1D conservation law, where on every cell two test functions are used. Define the local coordinate $\xi = (x - x_i)/\Delta x$. The test functions are

$$\phi_{i1} = 1/\Delta x, \quad \phi_{i2} = (x - x_i)/\Delta x^2 = \xi/\Delta x. \tag{7}$$

Because the numerical flux at half point $\hat{f}_{i+1/2}$ is always computed, from (3) the half discrete form can be written as

$$\begin{aligned} &\frac{dv_{i1}}{dt} + \frac{\hat{f}_{i+1/2} - \hat{f}_{i-1/2}}{\Delta x} = 0, \\ &\frac{dv_{i2}}{dt} + \frac{\hat{f}_{i+1/2} + \hat{f}_{i-1/2}}{2\Delta x} - V_i = 0, \end{aligned} \tag{8}$$

where

$$V_i = \langle f(u), \partial_x \phi_{i2} \rangle_{I_i} = \frac{1}{\Delta x} \int_{-1/2}^{1/2} f(\xi) d\xi$$

which is approximated by interpolation of different orders in schemes of corresponding orders.

2.1. The construction of 2nd-order WIBS

The order of the scheme is determined by the interpolation of $u(x)$ and $f(u)$. The construction of the scheme contains two steps:

Step 1: Interpolate function $u(x)$ to compute the numerical fluxes at specific points on the half cell.

Consider a stencil $\{I_i, I_{i+1}\}$, a 2nd-order interpolation of $u^-(\xi)$ is

$$\langle u(x), \phi_{i1} \rangle_{I_i} = v_{i,1}, \quad \langle u(x), \phi_{i2} \rangle_{I_i} = v_{i,2} \Rightarrow u^-(\xi) = v_{i,1} + 12 v_{i,2} \xi. \tag{9}$$

Thus we can approximate the function value at $x_{i+1/2}$:

$$u^-_{i+1/2} = v_{i,1} + 6 v_{i,2}. \tag{10}$$

$u^+_{i+1/2}$ is a mirror symmetric of $u^-_{i+1/2}$ with respect to $i + 1/2$:

$$u^+_{i+1/2} = v_{i+1,1} - 6 v_{i+1,2}. \tag{11}$$

With these $u^\pm_{i+1/2}$ and the local Lax–Friedrichs flux (5), $\hat{f}_{i+1/2}$ can be calculated.

Step 2: Interpolate $f(x)$ to obtain the volumetric integral.

From $\hat{f}_{i-1/2}$ and $\hat{f}_{i+1/2}$, $f(\xi)$ can be approximated to 2nd order:

$$f(\xi) = \frac{1}{2}(\hat{f}_{i-1/2} + \hat{f}_{i+1/2}) + (\hat{f}_{i+1/2} - \hat{f}_{i-1/2})\xi. \tag{12}$$

Then the volumetric integral in (8) is

$$V_i = \frac{1}{\Delta x} \int_{-1/2}^{1/2} f(\xi) d\xi = \frac{1}{\Delta x} \frac{\hat{f}_{i-1/2} + \hat{f}_{i+1/2}}{2}. \tag{13}$$

The substitution of this V_i into (8) yields the half discrete form. A TVD Runge–Kutta method is used to solve the ODE systems in time direction.

2.2. The construction of 3rd-order WIBS

A similar procedure can be done to construct a 3rd-order scheme.

Step 1: Interpolate function $u(x)$ to compute the numerical fluxes at specific points on the half cell.

Consider a stencil $\{I_i, I_{i+1}\}$, we can use $v_{i,1}$, $v_{i,2}$ and $v_{i+1,1}$ to approximate $u^-_{i+1/2}, u^-_{i+1/4}$, and $u^-_{i+3/4}$ to 3rd order:

$$\begin{aligned} u^-_{i+1/4} &= \frac{49}{48} v_{i,1} + \frac{13}{4} v_{i,2} - \frac{1}{48} v_{i+1,1}, \\ u^-_{i+1/2} &= \frac{5}{6} v_{i,1} + 4 v_{i,2} + \frac{1}{6} v_{i+1,1}, \\ u^-_{i+3/4} &= \frac{25}{48} v_{i,1} + \frac{13}{4} v_{i,2} + \frac{23}{48} v_{i+1,1}. \end{aligned} \tag{14}$$

And $u^+_{i+1/2}, u^+_{i+1/4}$, and $u^+_{i+3/4}$ can be constructed from $v_{i+1,1}, v_{i+1,2}$ and $v_{i,1}$ as:

$$\begin{aligned} u^+_{i+1/4} &= \frac{25}{48} v_{i+1,1} - \frac{13}{4} v_{i+1,2} + \frac{23}{48} v_{i,1}, \\ u^+_{i+1/2} &= \frac{5}{6} v_{i+1,1} - 4 v_{i+1,2} + \frac{1}{6} v_{i,1}, \\ u^+_{i+3/4} &= \frac{49}{48} v_{i+1,1} - \frac{13}{4} v_{i+1,2} - \frac{1}{48} v_{i,1}. \end{aligned} \tag{15}$$

Again the local Lax–Friedrichs flux (5) is used to compute $\hat{f}_{i+1/4}, \hat{f}_{i+1/2}$, and $\hat{f}_{i+3/4}$.

Step 2: Interpolate $f(x)$ to obtain the volumetric integral.

As in the construction of 2nd-order scheme, the same procedure leads to

$$V_i = \frac{1}{\Delta x} \int_{-1/2}^{1/2} f(\xi) d\xi = \frac{8(\hat{f}_{i-1/4} + \hat{f}_{i+1/4}) + \hat{f}_{i-1/2} + \hat{f}_{i+1/2}}{18 \Delta x}. \tag{16}$$

The substitution of this V_i into (8) yields the half discrete form. A TVD Runge–Kutta method is used to solve the ODE systems in time direction.

2.3. The construction of 4th-order WIBS

Step 1: Interpolate function $u(x)$ to compute the numerical fluxes at specific points on the half cell.

Consider a stencil $\{I_i, I_{i+1}\}$, we can use $v_{i,1}$, $v_{i,2}$, $v_{i+1,1}$ and $v_{i+1,2}$ to approximate $u_{i+1/2}$, $u_{i+1/4}$, and $u_{i+3/4}$ to 4th order (this time we construct a center scheme):

$$\begin{aligned} u_{i+1/4} &= \frac{131}{128}v_{i,1} + \frac{209}{64}v_{i,2} - \frac{3}{128}v_{i+1,1} + \frac{1}{64}v_{i+1,2}, \\ u_{i+1/2} &= \frac{1}{2}v_{i,1} + 2v_{i,2} + \frac{1}{2}v_{i+1,1} - 2v_{i+1,2}, \\ u_{i+3/4} &= -\frac{3}{128}v_{i,1} - \frac{1}{64}v_{i,2} + \frac{131}{128}v_{i+1,1} - \frac{209}{64}v_{i+1,2}. \end{aligned} \tag{17}$$

Substituting them into $f(u)$ yields the numerical fluxes at the corresponding points.

Step 2: Interpolate $f(x)$ to obtain the volumetric integral.

Here V_i is the same as in 3rd order scheme (16). The substitution of this V_i into (8) yields the half discrete form. A TVD Runge–Kutta method is used to solve the ODE systems in time direction.

2.4. The construction of 6th-order WIBS

Step 1: Interpolate function $u(x)$ to compute the numerical fluxes at specific points on the half cell.

Consider a stencil $\{I_{i-1}, I_i, I_{i+1}, I_{i+2}\}$, we can use $v_{i-1,1}$, $v_{i-1,2}$, $v_{i,1}$, $v_{i,2}$, $v_{i+1,1}$ and $v_{i+1,2}$ to approximate $u^-_{i+1/2}, u^-_{i+1/4}$, and $u^-_{i+3/4}$ to 6th order:

$$\begin{aligned} u^-_{i+1/4} &= \frac{1763}{110592}v_{i-1,1} + \frac{2741}{55296}v_{i-1,2} + \frac{3223}{3072}v_{i,1} + \frac{102391}{27648}v_{i,2} - \frac{7199}{110592}v_{i+1,1} + \frac{12137}{55296}v_{i+1,2}, \\ u^-_{i+1/2} &= \frac{13}{108}v_{i-1,1} + \frac{25}{54}v_{i-1,2} + \frac{7}{12}v_{i,1} + \frac{241}{54}v_{i,2} + \frac{8}{27}v_{i+1,1} - \frac{28}{27}v_{i+1,2}, \\ u^-_{i+3/4} &= \frac{239}{4096}v_{i-1,1} + \frac{1451}{6144}v_{i-1,2} + \frac{7}{3072}v_{i,1} + \frac{3277}{3072}v_{i,2} + \frac{11543}{12288}v_{i+1,1} - \frac{17665}{6144}v_{i+1,2}. \end{aligned} \tag{18}$$

And $u^+_{i+1/2}, u^+_{i+1/4}$, and $u^+_{i+3/4}$ are a mirror symmetric of them with respect to $i+1/2$:

$$\begin{aligned} u^+_{i+1/4} &= \frac{239}{4096}v_{i+2,1} - \frac{1451}{6144}v_{i+2,2} + \frac{7}{3072}v_{i+1,1} - \frac{3277}{3072}v_{i+1,2} + \frac{11543}{12288}v_{i,1} + \frac{17665}{6144}v_{i,2}, \\ u^+_{i+1/2} &= \frac{13}{108}v_{i+2,1} - \frac{25}{54}v_{i+2,2} + \frac{7}{12}v_{i+1,1} - \frac{241}{54}v_{i+1,2} + \frac{8}{27}v_{i,1} + \frac{28}{27}v_{i,2}, \\ u^+_{i+3/4} &= \frac{239}{4096}v_{i+2,1} - \frac{1451}{6144}v_{i+2,2} + \frac{7}{3072}v_{i+1,1} - \frac{3277}{3072}v_{i+1,2} + \frac{11543}{12288}v_{i,1} + \frac{17665}{6144}v_{i,2}. \end{aligned} \tag{19}$$

Again the local Lax–Friedrichs flux (5) is used to compute $\hat{f}_{i+1/4}, \hat{f}_{i+1/2}$, and $\hat{f}_{i+3/4}$.

Step 2: Interpolate $f(x)$ to obtain the volumetric integral.

The same procedure as in the construction of 2nd-order scheme leads to:

$$V_i = \frac{1}{\Delta x}\int_{-1/2}^{1/2} f(\xi)d\xi = \frac{3(\hat{f}_{i-3/4} + \hat{f}_{i+3/4}) + 205(\hat{f}_{i-1/4} + \hat{f}_{i+1/4}) + 17(\hat{f}_{i-1/2} + \hat{f}_{i+1/2})}{450\Delta x}. \tag{20}$$

The substitution of this V_i into (8) yields the half discrete form. A TVD Runge–Kutta method is used to solve the ODE systems in time direction.

2.5. The construction of 10th-order WIBS

Step 1: Interpolate function $u(x)$ to compute the numerical fluxes at specific points on the half cell.

We consider a stencil $\{I_{i-2}, I_{i-1}, I_i, I_{i+1}, I_{i+2}, I_{i+3}\}$. Then $u^\pm_{i+1/2}, u^\pm_{i+1/6}, u^\pm_{i+1/3}, u^\pm_{i+2/3}$, and $u^\pm_{i+5/6}$ can be approximated to the 10th order, which are given in the Appendix.

Again the local Lax–Friedrichs flux (5) is used to compute $\hat{f}_{i+1/6}$, $\hat{f}_{i+1/3}$, $\hat{f}_{i+1/2}$, $\hat{f}_{i+2/3}$, and $\hat{f}_{i+5/6}$.

Step 2: Interpolate $f(x)$ to obtain the volumetric integral.

The same procedure as in the construction of 2nd-order scheme leads to:

$$\begin{aligned} V_i = \frac{1}{1058400\Delta x}\Big[&1045(\hat{f}_{i-5/6} + \hat{f}_{i+5/6}) - 11584(\hat{f}_{i-2/3} + \hat{f}_{i+2/3}) + 115008(\hat{f}_{i-1/3} + \hat{f}_{i+1/3}) + 316974(\hat{f}_{i-1/6} + \hat{f}_{i+1/6}) \\ &+107757(\hat{f}_{i-1/2} + \hat{f}_{i+1/2})\Big]. \end{aligned} \tag{21}$$

The substitution of this V_i into (8) yields the half discrete form. A TVD Runge–Kutta method is used to solve the ODE systems in time direction.

2.6. A stability analysis

For linear convection equation where $f(u) = au$, a = const., $a > 0$, a Fourier analysis of the stability of WIBS can be carried out analytically. To demonstrate the precess we consider the 3rd-order WIBS. Because $a > 0$, only $u^-_{i+1/2}, u^-_{i+1/4}$, and $u^-_{i+3/4}$ are to be computed, and at every point there is $\hat{f} = au^-$. Thus the final half discrete form can written as:

$$\begin{aligned} &\frac{dv_{i1}}{dt} + \frac{a}{6\Delta x}[-5v_{i-1,1} + 4v_{i,1} + v_{i+1,1} + 24(v_{i,2} - v_{i-1,2})] = 0, \\ &\frac{dv_{i2}}{dt} + \frac{a}{36\Delta x}[5v_{i-1,1} - 8v_{i,1} + 3v_{i+1,1} + 12(v_{i-1,2} + v_{i,2})] = 0. \end{aligned} \tag{22}$$

Assume

$$v_{i,1} = A(t)e^{jkx_i}, \quad v_{i,2} = B(t)e^{jkx_i},$$

where $j = \sqrt{-1}$, and substitute them into (22), it easily follows that

$$A(t) = C_1 \exp\left[\frac{r_1(c)at}{\Delta x}\right] + C_2 \exp\left[\frac{r_2(c)at}{\Delta x}\right], \quad c = k\Delta x; \tag{23}$$

where C_1 and C_2 are two constants and

$$r_1(c) = -\frac{1}{12}e^{jc} - \frac{1}{2} + \frac{1}{4}e^{-jc} + M, \quad r_2(c) = -\frac{1}{12}e^{jc} - \frac{1}{2} + \frac{1}{4}e^{-jc} - M; \quad M = \frac{1}{12}\sqrt{e^{2jc} + 52e^{jc} - 186 + 180e^{-jc} - 31e^{-2jc}}.$$

The Taylor expansions of $r_1(c)$ and $r_2(c)$ are

$$r_1(c) = -jc + \frac{3}{40}jc^5 - \frac{1}{8}c^6 + O(c^7), \quad r_2(c) = -\frac{2}{3} + \frac{1}{3}jc + O(c^2).$$

Thus when $c \to (\Delta x \to 0)$, $A(t) \to C_1 e^{-jkat}$, which recovers the exact solution. The lowest-order real parts of $r_1(c)$ and $r_2(c)$ are $-\frac{1}{8}c^6$ and $-\frac{2}{3}$, respectively, implying that in (23) the second term diminishes very quickly with the increase of t, and the first term diminishes too when c is small enough. Thus the scheme is stable for small c. Fig. 1 shows the distribution of the real parts of $r_1(c)$ and $r_2(c)$, which are never greater than 0. Hence $A(t)$ will not grow for arbitrary $c \geqslant 0$. While it is easy to derive

$$\frac{dB}{dt} = -\frac{1}{3}(1 + e^{-jc})B(t) + \frac{1}{36}(8 - 3e^{jc} - 5e^{-jc})A(t).$$

When $A(t)$ diminishes, because $-\frac{1}{3}\Re(1 + e^{-jc}) \leqslant 0$, $B(t)$ will decrease too. Thus *the half discrete form of 3rd-order WIBS is unconditionally stable for arbitrary c*. Of course, as to the stability of the scheme, the method for time integration should be considered too. But the present analysis shows that if the time integration is accurate enough, 3rd-order WIBS can achieve high stability, which has been validated by the numerical experiment in the stability test to be reported in Section 4.

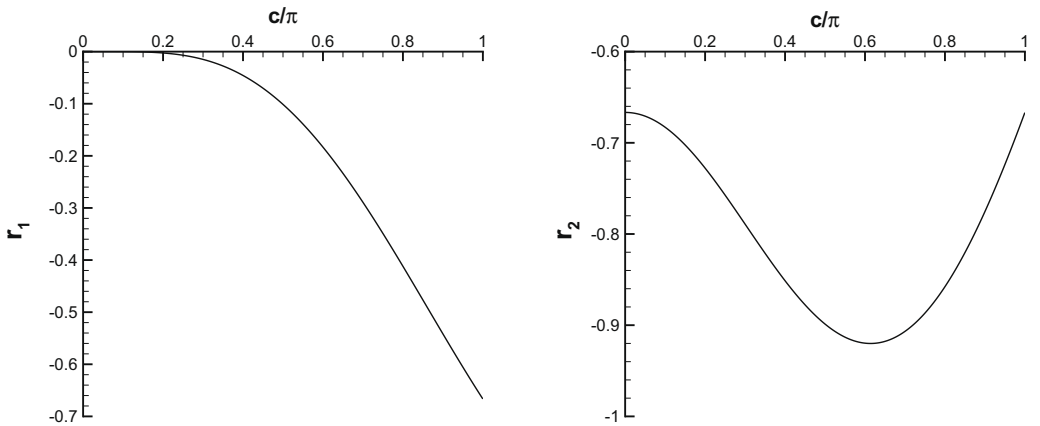

Fig. 1. The distribution of the real parts of $r_1(c)$ (left) and $r_2(c)$ (right). $c \in [0, \pi]$.

3. The construction of WENO-WIBS

A weighted essentially non-oscillatory (WENO) method is applied to WIBS (WENO-WIBS) in the reconstruction of $u(x)$ to capture the discontinuity or large gradient field. Different designed WENO can be constructed for schemes of different orders in the preceding section. Specifically, we present here the WENO construction for the 6th- and 10th-order scheme.

3.1. The 6th-order WENO-WIBS

Consider the 6th-order WENO-WIBS (WENO-WIBS6) first. For the basic 6th-order stencil $S_0 = \{v_{i-1,1}, v_{i-1,2}, v_{i,1}, v_{i,2}, v_{i+1,1}, v_{i+1,2}\}$, we choose the following sub-stencils

$$\begin{aligned} &S_1 = \{v_{i-1,1}, v_{i-1,2}, v_{i,1}, v_{i,2}\}, \quad S_2 = \{v_{i-1,1}, v_{i-1,2}, v_{i,1}, v_{i+1,1}\}, \\ &S_3 = \{v_{i,1}, v_{i,2}, v_{i+1,1}, v_{i+1,2}\}, \quad S_4 = \{v_{i,1}, v_{i+1,1}, v_{i+2,1}, v_{i+2,2}\} \end{aligned} \tag{24}$$

to approximate $u^-(x)$ *up to the 3rd order with least-square interpolation* respectively. Denote approximate result as $u_j(x)^-$ ($j = 1, 2, 3, 4$) for each sub-stencil S_j. The 6th-order approximation of $u^-(x)$ on S_0 is denoted by $u_0(x)^-$. We compute the smoothness indicator for each sub-stencil, denoted by β_j, which measures how smooth the function $u_j(x)^-$ is on the sub-cell $[x_i, x_{i+1}]$. The smaller this smoothness indicator β_j, the smoother the function $u_j(x)^-$ is in the sub-cell. We use the same recipe for the smoothness indicator as in [8]:

$$\beta_j = \sum_{k=1}^{2} \int_{x_{i-1/2}}^{x_{x+1/2}} \Delta x^{2k-1} \left[\partial_x^k u_j(x)^-\right]^2 dx. \tag{25}$$

In the actual numerical implementation the smoothness indicators β_j are written out explicitly as quadratic forms of the cell recordings $v_{i,m}$:

$$\begin{aligned} \beta_1 &= \left[-\frac{216}{37} v_{i-1,2} + \frac{36}{37}(v_{i,1} - v_{i-1,1}) + \frac{228}{37} v_{i,2}\right]^2 + \frac{13}{3}\left[6(v_{i-1,2} + v_{i,2})\right]^2, \\ \beta_2 &= \left(-\frac{149}{301} v_{i-1,1} + \frac{12}{301} v_{i-1,2} - \frac{2}{301} v_{i,1} + \frac{151}{301} v_{i+1,1}\right)^2 + \frac{13}{3}\left(\frac{283}{602} v_{i-1,1} - \frac{72}{301} v_{i-1,2} - \frac{289}{301} v_{i,1} + \frac{295}{602} v_{i+1,1}\right)^2, \\ \beta_3 &= \left[\frac{228}{37} v_{i,2} + \frac{36}{37}(v_{i+1,1} - v_{i,1}) - \frac{216}{37} v_{i+1,2}\right]^2 + \frac{13}{3}\left[6(v_{i,2} - v_{i+1,2})\right]^2, \\ \beta_4 &= \left(-\frac{446}{301} v_{i,1} + \frac{580}{301} v_{i+1,1} - \frac{134}{301} v_{i+2,1} - \frac{132}{301} v_{i+2,2}\right)^2 + \frac{13}{3}\left(\frac{295}{602} v_{i,1} - \frac{289}{301} v_{i+1,1} + \frac{283}{602} v_{i+2,1} + \frac{72}{301} v_{i+2,2}\right)^2. \end{aligned} \tag{26}$$

The nonlinear weights are defined as

$$\omega_j = \frac{\bar{\omega}_j}{\sum_k \bar{\omega}_k}, \quad \bar{\omega}_k = \frac{1}{(\epsilon + \beta_k)^2}, \tag{27}$$

where ϵ is a small number to avoid the denominator to become *0*. We use $\epsilon = 10^{-6}$ for all computations in this paper. ω_j are used to select sub-stencil. To realize the transition from sub-stencils S_j to the whole stencil S_0 in the smooth region, define new weights as

$$\tilde{\omega}_1 = \tilde{\omega}(s), \quad \tilde{\omega}_2 = 1 - \tilde{\omega}_1; \qquad s = \frac{N}{N-1} \sum_{k=1}^{N} (\omega_k - 1/N)^2, \tag{28}$$

where $N = 4$ is the number of the sub-stencils. Here $s = 0$ means the sub-stencils have equal weights and the function in the neighboring region is smooth; and $s = 1$ meas one sub-stencil has largest sub-stencil weight with $\omega = 1$, namely the function in the neighboring region contains discontinuity. Hence the magnitude of s reflects the deviation of the function from a smooth one. The function $\tilde{\omega}(s)$ ($\geqslant 0$) satisfies:

$$\tilde{\omega}(0) = 0, \quad \tilde{\omega}(1) = 1; \qquad \left.\frac{d\tilde{\omega}}{ds}\right|_{s=0} = \left.\frac{d\tilde{\omega}}{ds}\right|_{s=1} = 0. \tag{29}$$

Here we choose it to be

$$\frac{d\tilde{\omega}_{mn}}{ds} = \frac{\Gamma(m+n+2)}{\Gamma(m+1)\Gamma(n+1)} s^m (1-s)^n, \quad m, n \in \mathbb{N}, \tag{30}$$

where $\Gamma(x)$ is the Gamma function. Obviously, this $\tilde{\omega}_{mn}(s)$ satisfies (29). For schemes of certain orders, sometimes m should be greater than a special natural number. With numerical experiments we found that $\tilde{\omega}_{mn}(s)$ can be set as $\tilde{\omega}_{32}(s) = s^4(10s^2 - 24s + 15)$.

With these weights, the final interpolation of $u^-(x)$ is obtained by

$$u^-(x) = \tilde{\omega}_1 \sum_{k=1}^{N} \omega_k u_k(x)^- + \tilde{\omega}_2 u_0^-(x). \tag{31}$$

Thus when $s = 0, \tilde{\omega}_1 = 0, \tilde{\omega}_2 = 1, u^-(x) = u_0(x)^-$; when $s = 1, \tilde{\omega}_1 = 1, \tilde{\omega}_2 = 0, u^-(x) = \sum_{k=1}^{N} \omega_k u_k(x)^-$ which realizes the selection of the smoothest sub-stencil. Fig. 2 gives the shapes of $\tilde{\omega}_{12}(s), \tilde{\omega}_{21}(s)$ and $\tilde{\omega}_{32}(s)$.

From $u^-(x)$ in (31) we can obtain $u^-_{i+1/4}, u^-_{i+1/2}$, and $u^-_{i+3/4}$, whose mirror symmetric with respect to $j + 1/2$ are $u^+_{i+1/4}, u^+_{i+1/2}$, and $u^+_{i+3/4}$. The rest procedures are the same as in the construction of 6th-order WIBS. It is easily proven that *this construction of weighted interpolation can keep excellent accuracy in smooth region*. The order of accuracy will be examined numerically in Section 4.

3.2. Tenth-order WENO-WIBS

A similar procedure is constructed for 10th-order WENO-WIBS (WENO-WIBS10). We use the same sub-stencils as in WENO-WIBS6, but change S_0 to the stencil of WIBS10. Thus the weights and the combination procedure are the same as in WENO-WIBS6. The only difference is that there are five point-values to compute $u^{\pm}_{i+1/2}$, $u^{\pm}_{i+1/6}$, $u^{\pm}_{i+1/3}$, $u^{\pm}_{i+2/3}$, and $u^{\pm}_{i+5/6}$.

For systems of conservation laws, such as the Euler equations of gas dynamics, the reconstructions are all performed in the local characteristic directions to avoid oscillation; see, e.g. [5] for details.

4. Numerical validations

In this section we present the results of our numerical experiments for nth-order WIBS (WIBSn) and WENO-WIBSn with 3rd order TVD Runge–Kutta method in time direction. These results are compared with 6th-order Hermite upwind WENO scheme (HCWENO6) in [4] and 5th-order finite-volume WENO schemes (WENO5) in [5]. An uniform mesh with N cells is used for all tests. Although the WIBSs and WENO-WIBSs are found to be highly stable, to realize the high spatial accuracy the time step should be small enough, as will soon be shown in the accuracy tests. Hence we choose CFL = 0.1 for all of the computation experiments except for stability and accuracy tests.

4.1. Stability tests

With numerical experiments on the linear convection equation we found the critical CFL numbers of the 2nd $\sim$ 10th-order WIBS, which are shown in Table 1. We can see that WIBS is highly stable. The critical CFL number decreases slightly with the increasing of the scheme order (note that because WIBS4 is a center scheme, it has lower critical CFL).

4.2. Accuracy tests

In this subsection we test the accuracy of WENO-WIBS6 and WENO-WIBS10 on nonlinear scalar problems and nonlinear systems.

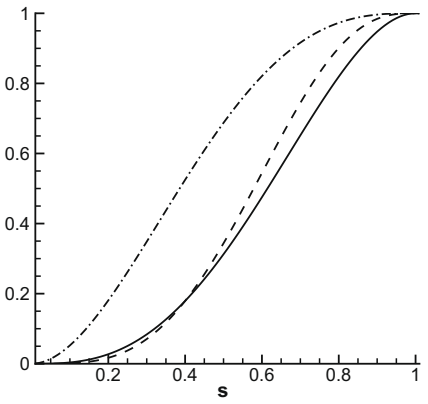

Fig. 2. The shape of $\tilde{\omega}_{mn}(s)$. Dashdot: $\tilde{\omega}_{12}(s)$; solid: $\tilde{\omega}_{21}(s)$; and dashed: $\tilde{\omega}_{32}(s)$.

Table 1
Critical CFL numbers of the 2nd $\sim$ 10th-order WIBS for linear convection equation.

	WIBS2	WIBS3	WIBS4	WIBS6	WIBS10
CFL	0.942	1.269	0.538	0.662	0.539

Table 2
Burgers equation; $u(x,0) = 1/2 + \sin(\pi x)$; periodic boundary conditions. Compare the accuracy of WENO-WIBS6 and HCWENO6 [4].

N	WENO-WIBS6					HCWENO6			
	L_1 error	Order	L_∞ error	Order	Max(CFL)	L_1 error	Order	L_∞ error	Order
10	1.16E−3	–	7.91E−3	–	0.40	2.51E−4	–	5.81E−4	–
20	3.97E−5	4.9	3.43E−4	4.5	0.20	3.18E−5	3.0	1.42E−4	2.0
40	8.85E−7	5.5	1.05E−5	5.0	9.0E−2	9.36E−7	5.1	6.03E−6	4.6
80	1.34E−8	6.0	1.84E−7	5.8	3.8E−2	2.14E−8	5.4	1.57E−7	5.3
160	2.17E−10	5.9	3.17E−9	5.8	1.8E−2	4.20E−10	5.7	3.47E−9	5.5
320	5.59E−12	5.3	8.03E−11	5.3	9.0E−3	7.30E−12	5.9	6.18E−11	5.8

Example 1. Solve the nonlinear scalar Burgers equation

$$u_t + \left(\frac{u^2}{2}\right)_x = 0 \tag{32}$$

with the initial condition $u(x,0) = 0.5 + \sin(\pi x)$, and a *2*-periodic boundary condition. When $t = 0.5/\pi$ the solution is still smooth. The errors and numerical orders of accuracy by WENO-WIBS6 and HCWENO6 [4] are shown in Table 2. We can see that WENO-WIBS6 achieves its designed order of accuracy, with slightly smaller errors than those of HCWENO6. Because the time discretization is 3rd order, to exhibit the spatial accuracy, time step should be small enough. In Table 2 we also give the maximum CFLs to achieve the corresponding errors.

The errors of WENO-WIBS10 are shown in Table 3. But this time the designed order cannot be recovered. Perhaps the designed accuracy can be recovered only if the grid size is sufficiently small. But when the grid number $N > 80$, the errors will be too small for double-precision real number. So we stop the verification of the accuracy of WNO-WIBS10 here.

Example 2. Solve the nonlinear system of Euler equations

$$u_t + f(u)_x = 0 \tag{33}$$

with

$$u = (\rho, \rho v, E)^T, \quad f(u) = (\rho v, \rho v^2 + p, v(E+p))^T.$$

Here ρ is the density, v is the velocity, E is the total energy, p is the pressure, which is related to the total energy by $E = p/(\gamma - 1) + \rho v^2/2$ with $\gamma = 1.4$. The initial condition is set to be $\rho(x,0) = 1 + 0.2\sin(\pi x)$, $v(x,0) = 1$, $p(x,0) = 1$, with a 2-periodic boundary condition. The exact solution is $\rho(x,t) = 1 + 0.2\sin[\pi(x-t)]$, $v(x,t) = p(x,t) = 1$. We compute the solution up to $t = 2$. The errors and numerical orders of accuracy of the density ρ for WENO-WIBS6 are shown in Table 4, in comparison with the results of HCWENO6 [4]. We can see that the errors of WENO-WIBS6 are about two orders smaller those of HCWENO6 and its designed order of accuracy is perfectly recovered (when $N = 160$ the error is approaching the machine error for double-precision real number, so the order of accuracy does not show the designed one).

4.3. Resolution for short waves

It is well known that WENO schemes are diffusive for short waves. To see the ability of WENO-WIBS in capturing short waves we have done the following experiment.

Table 3
Burgers equation; $u(x,0) = 1/2 + \sin(\pi x)$; periodic boundary conditions. The errors of WENO-WIBS10.

N	L_1 error	Order	L_∞ error	Order	Max(CFL)	N	L_1 error	Order	L_∞ error	Order	Max(CFL)
10	4.66E−4		3.70E−3		2.4E−2	40	5.00E−8	7.3	7.26E−7	7.0	8.0E−4
20	7.84E−6	5.9	9.45E−5	5.3	1.2E−3	80	6.13E−11	9.7	1.26E−9	6.9	6.0E−4

Table 4
One-dimensional Euler equations; $\rho(x,0) = 1 + 0.2\sin(\pi x)$, $u(x,0) = 1$, $p(x,0) = 1$; periodic boundary conditions, $t = 2$; L_1 and L_∞ errors of density ρ. Compare the accuracy of WENO-WIBS6 and HCWENO6 [4].

N	WENO-WIBS6				HCWENO6			
	L_1 error	Order	L_∞ error	Order	L_1 error	Order	L_∞ error	Order
10	5.31E−6	–	1.12E−5	–	7.15E−4	–	5.59E−4	–
20	4.41E−8	6.9	7.30E−8	7.3	8.92E−6	6.2	7.00E−6	6.3
40	3.98E−10	6.8	6.34E−10	6.8	1.21E−7	6.2	9.49E−8	6.2
80	4.24E−12	6.5	6.76E−12	6.6	1.75E−9	6.1	2.12E−9	6.1
160	1.27E−13	5.1	5.11E−13	3.7	3.14E−11	6.0	3.80E−11	6.0

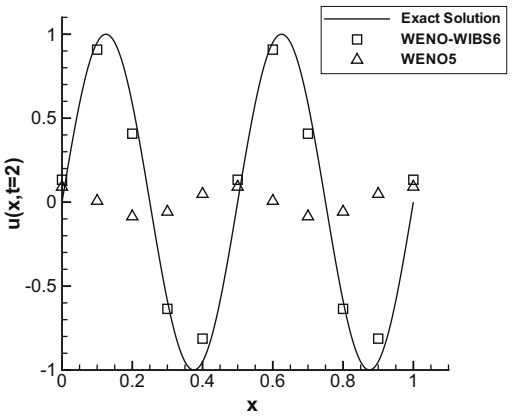

Fig. 3. Compare the diffusion of WENO-WIBS6 and WENO5 for computing linear convection equation with sine wave initial condition and periodic boundary conditions. $N = 10$ cells, $t = 2$.

Example 3. Solve the linear convection equation:

$$u_t + u_x = 0, \quad x \in [0,1], \tag{34}$$

with the initial condition:

$$u(x,0) = \sin(4\pi x). \tag{35}$$

The cell number $N = 10$, $t = 2$, with periodic boundary conditions. The results of WENO-WIBS6 and WENO5 are compared in Fig. 3. Here only five cells are used for every period of sine wave. Obviously, WENO-WIBS6 has a much higher resolution than WENO5 in capturing short waves.

4.4. Test cases with discontinuities

To test the ability of WENO-WIBS6 and WENO-WIBS10 in capturing discontinuities, we have performed the following numerical experiments.

Example 4. Solve the linear convection equation(34) with a discontinuous initial condition:

$$u(x,0) = 1, \text{ for } \quad x \in (0.25, 0.75), \qquad u(x,0) = 0, \quad \text{for } x \in [0, 0.25] \cup [0.75, 1], \tag{36}$$

and a periodic boundary condition. We compare the results obtained by WENO-WIBS6 and WENO-WIBS10 with WENO5 at $t = 1$ and $t = 20$, respectively. The results are shown in Figs. 4 and 5, where the regions adjacent to the discontinuities are zoomed in and exhibited. Compared to WENO5, for capturing discontinuity WENO-WIBS6 and WENO-WIBS10 have higher resolution and smaller numerical oscillation.

Example 5. Solve the same nonlinear Burgers equation (32) as in Example 1 with the same initial and boundary conditions, except that we now compute the results at $t = 1.5/\pi$ when a schock has already appeared in the solution. See Fig. 6 (left and center), WENO-WIBS6 and WENO-WIBS10 give non-oscillation shock transitions for this problem.

Example 6. Solve the nonlinear non-convex scalar Buckley–Leverett problem

$$u_t + \left[\frac{4u^2}{4u^2 + (1-u)^2}\right]_x = 0 \tag{37}$$

with the initial data $u = 1$ when $1/2 \leqslant x \leqslant 1$ and $u = 0$ elsewhere. The solution is computed up to $t = 0.4$. The exact solution is a shock–rarefaction–contact discontinuity mixture. Some high order schemes may fail to converge to the correct entropy solution for this problem. As shown in Fig. 6 (right), WENO-WIBS6 gives good resolution to the correct entropy solution for this problem.

Example 7. Solve the Euler equations (33) with Riemann initial condition for Lax problem

$$(\rho, v, p) = (0.445, 0.698, 3.528) \quad \text{for } x \in [-5, 0], \qquad (\rho, v, p) = (0.5, 0, 0.571) \quad \text{for } x \in (0, 5]. \tag{38}$$

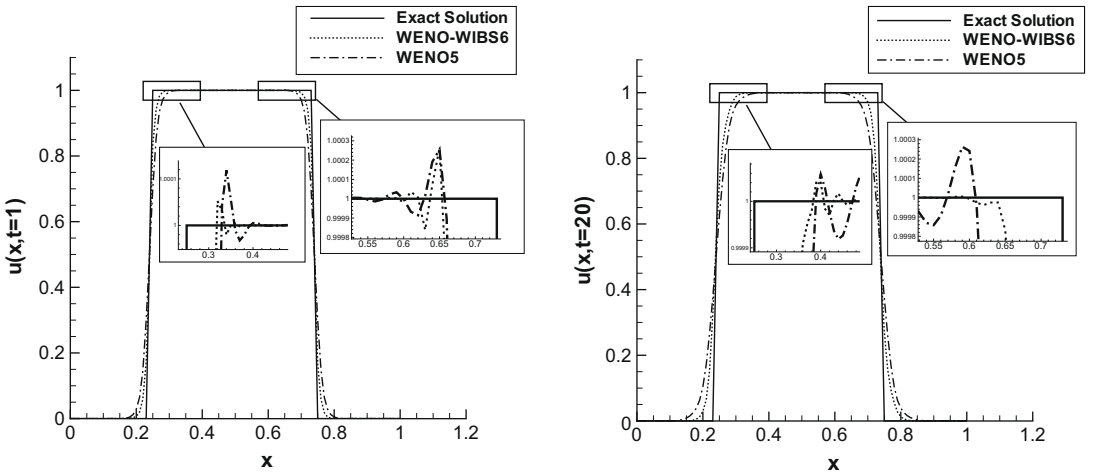

Fig. 4. The results of WENO-WIBS6 and WENO5 for computing linear convection equation with square wave initial condition and periodic boundary condition. $N = 100$ cells, $t = 1$ and $t = 20$.

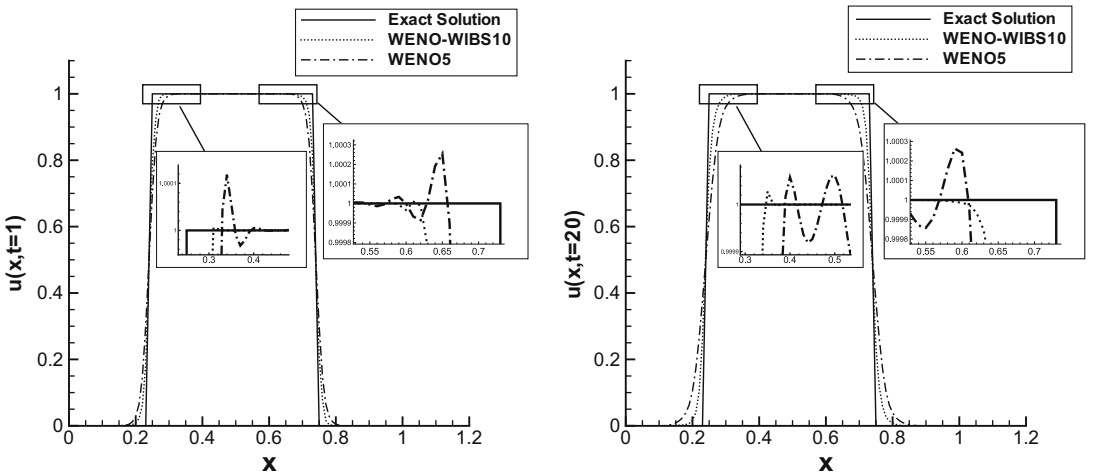

Fig. 5. The results of WENO-WIBS10 and WENO5 for computing linear convection equation with square wave initial condition and periodic boundary condition. $N = 100$ cells, $t = 1$ and $t = 20$.

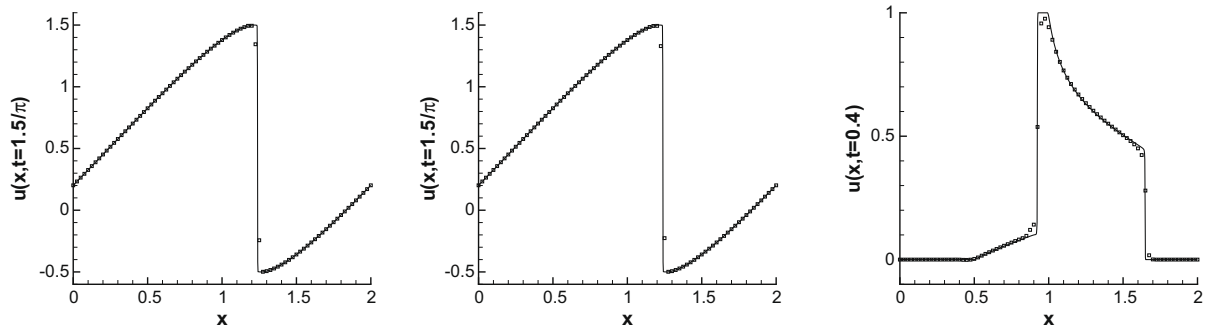

Fig. 6. Left: Burgers equation. $u(x,0) = 0.5 + \sin(\pi x)$. $t = 1.5/\pi$, WENO-WIBS6. Center: Burgers equation. $u(x,0) = 0.5 + \sin(\pi x)$. $t = 1.5/\pi$, WENO-WIBS10. Right: Buckley–Leverett problem. $t = 0.4$. For all figures $N = 80$ cells. Solid line: exact solution; squares: computed solution.

The computation is run up to $t = 1.3$. Set the cell number $N = 200$. In Fig. 7, the left plot is the density obtained by WENO-WIBS6 (square), compared to that obtained by WENO5 (square) on the right. And Fig. 8 shows the results of WENO-WIBS10. The solid curves in Figs. 7–10 are exact solutions [22]. Figs. 9 and 10 give the computed velocity and pressure by WENO-WIBS6 and WENO-WIBS10 against the accurate solution. From these figures we can see that both WENO-WIBS6 and

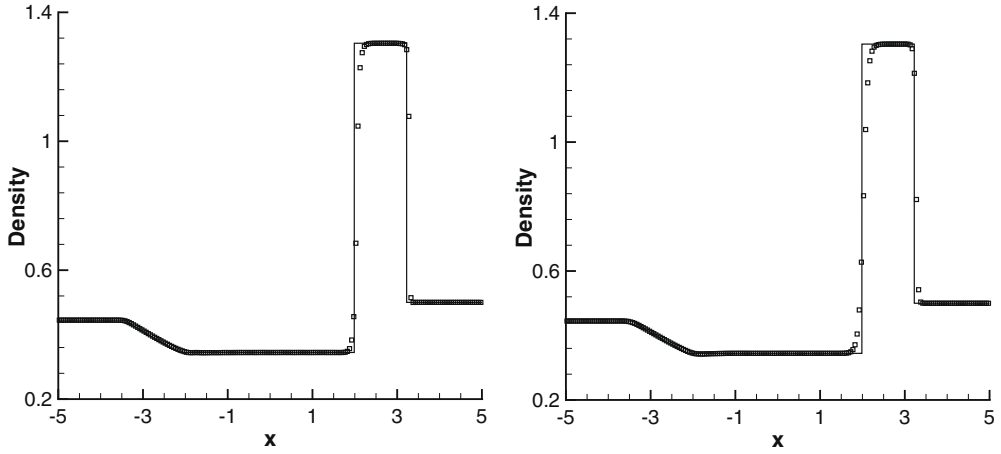

Fig. 7. The Lax problem. $t = 1.3$. WENO-WIBS6 (left) and WENO5 (right), $N = 200$ cells. Density ρ. Solid line: exact solution and squares: computed solution.

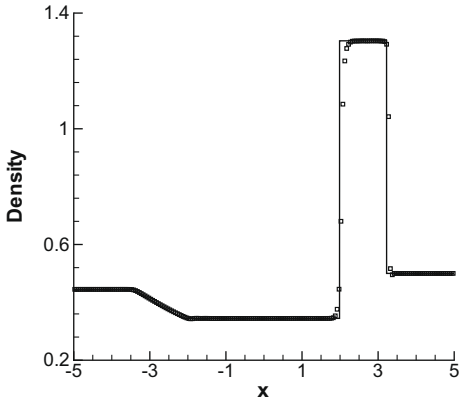

Fig. 8. The Lax problem. $t = 1.3$. WENO-WIBS10, $N = 200$ cells. Density ρ. Solid line: exact solution and squares: computed solution.

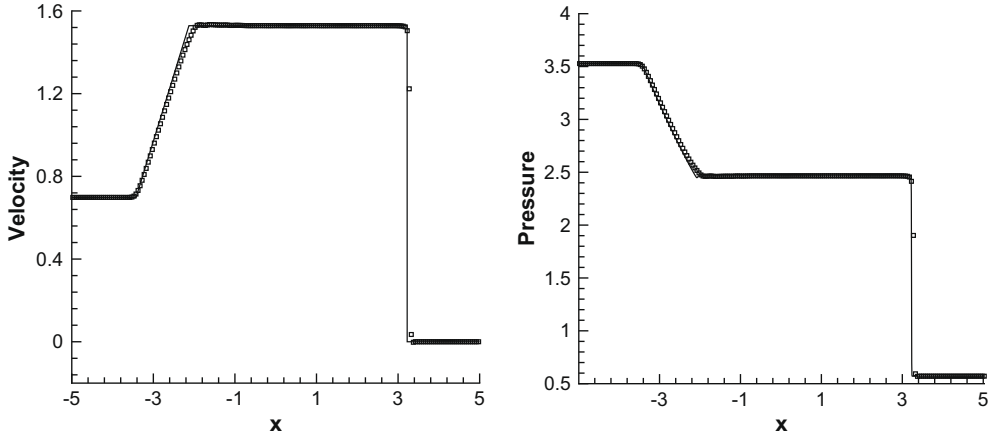

Fig. 9. The Lax problem. $t = 1.3$. Velocity (left) and pressure (right) obtained by WENO-WIBS6, $N = 200$ cells. Solid line: exact solution and squares: computed solution.

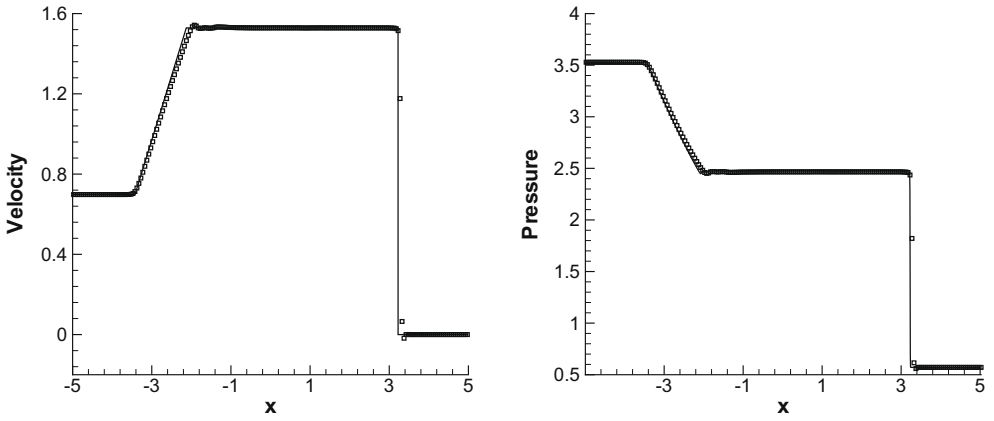

Fig. 10. The Lax problem. $t = 1.3$. Velocity (left) and pressure (right) obtained by WENO-WIBS10, $N = 200$ cells. Solid line: exact solution and squares: computed solution.

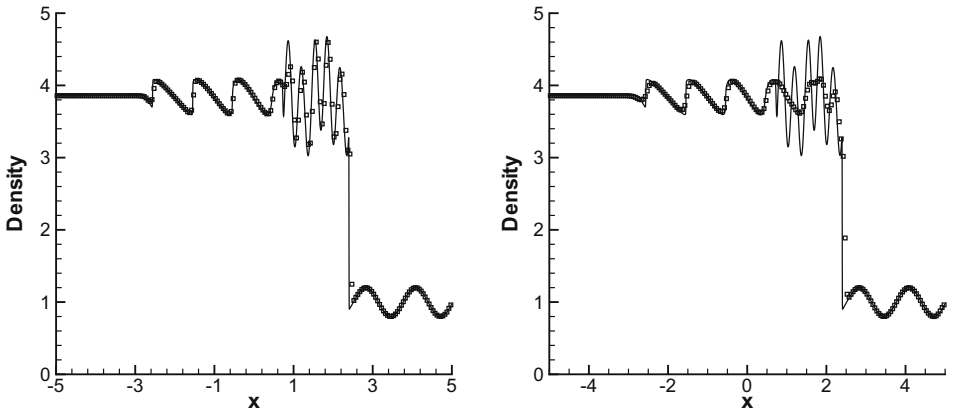

Fig. 11. The shock density wave interaction problem. $t = 1.8$. WENO-WIBS6 (left) and WENO5 (right), $N = 200$ cells. Density ρ. Solid line: "exact solution" and squares: computed solution.

WENO-WIBS10 have higher resolution than WENO5 in capturing discontinuities, just like in the computation of linear convection equation with square-wave initial condition; and numerical oscillations have been effectively suppressed. But the results of WENO-WIBS10 exhibit small numerical oscillations near discontinuities.

The preceding examples contain only shocks and simple smooth region solutions (almost piecewise linear), for which shock resolution is the main concern and usually a good 2nd-order non-oscillation scheme would give satisfactory results. There is little advantage in using higher order schemes except for a higher resolution of discontinuities. These numerical experiments are used mainly to demonstrate the non-oscillatory property of WENO-WIBS6 and 10. A higher-order scheme would show its advantage when the solution contains both shocks and complex smooth region structures. A typical example is the problem of shock interaction with entropy waves (Shu–Osher problem) [18].

Example 8. We solve the Euler equations (33) with a moving Mach 3 shock interacting with sine waves in density, i.e. initially

$$\begin{aligned}(\rho, v, p) &= (3.857143, 2.629369, 10.333333) \quad \text{for } x < -4,\\ (\rho, v, p) &= (1 + 0.2\sin(5x), 0, 1) \quad \text{for } x \geqslant -4.\end{aligned} \tag{39}$$

The computed density ρ is plotted at $t = 1.8$ against the reference solution, obtained by WENO5 on $N = 3000$ cells. We compare the results of WENO-WIBS6 and WENO5 in Fig. 11 ($N = 200$) and Fig. 12 ($N = 300$). And the results of WENO-WIBS10 are shown in Fig. 13: left ($N = 200$), right ($N = 300$).

As shown in these figures, WENO-WIBS6 and 10 have better performance than WENO5 in the smooth region with complex structures—the resolution of WENO-WIBS6 on $N = 200$ cells is even better than that of WENO5 on $N = 300$ cells. The resolution of WENO-WIBS10 for short waves is better than that of WENO-WIBS6.

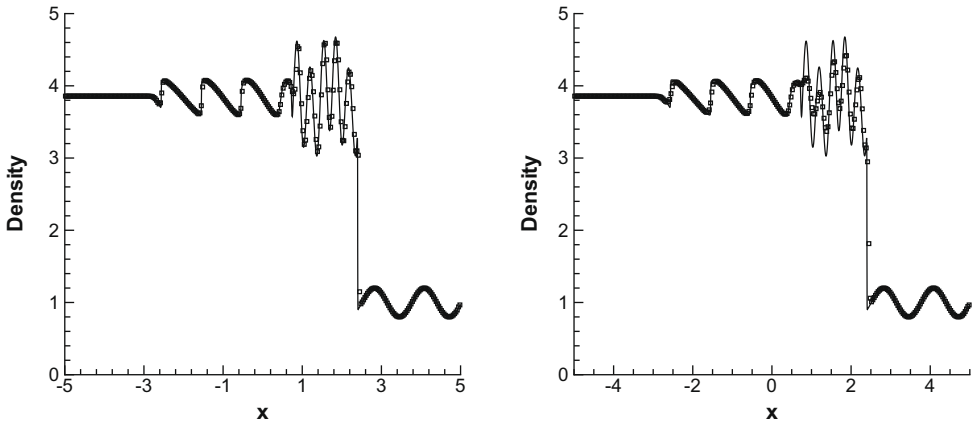

Fig. 12. The shock density wave interaction problem. $t = 1.8$. WENO-WIBS6 (left) and WENO5 (right), $N = 300$ cells. Density ρ. Solid line: "exact solution" and squares: computed solution.

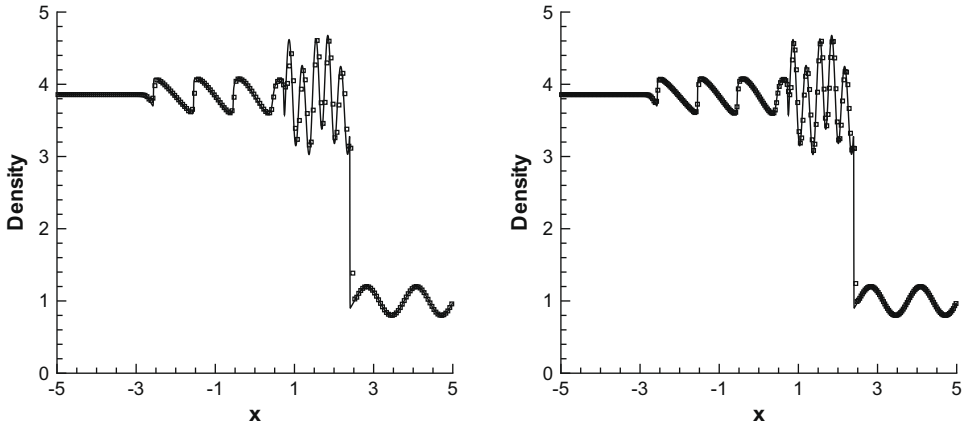

Fig. 13. The shock density wave interaction problem. $t = 1.8$. Results of WENO-WIBS10 on $N = 200$ (left) and $N = 300$ (right), respectively. Density ρ. Solid line: "exact solution" and squares: computed solution.

5. Concluding remarks

In this paper, we have constructed a new class of weighted integral based scheme (WIBS), where the integral of the function with a set of linearly independent test functions are recorded on every cell. An appropriate choice of the test functions and interpolation methods can recover many existing schemes.

With proper test functions and interpolation methods, we have constructed a class of WIBS and WENO-WIBS, where the time integration is performed with TVD Runge–Kutta procedures. The analytical and numerical investigations show that:

1. The high-order WIBS are highly stable.
2. In smooth region, the designed order of accuracy of WENO-WIBS is achieved successfully for nonlinear hyperbolic conservation-law systems.
3. Owing to the compactness of WENO-WIBS interpolating stencil, compared to WENO5 the WENO-WIBS6 has higher resolution for capturing the discontinuity and short waves in smooth region. The numerical oscillations near the discontinuity are extensively suppressed.
4. The computational cost of WENO-WIBS6 is about 4/3 times that of WENO5 scheme on the same grid.

Since it is straightforward to add cell recordings (just by adding test functions), WIBS and WENO-WIBS can easily retain accuracy near the boundary. But we have presently confined our work to the problems with trivial boundary conditions and left this issue to future work. Moreover, both WIBS and WENO-WIBS are constructed on a finite-volume formulation, and hence can be readily extended to unstructured meshes and multi-dimensional problems. These extensions will be reported separately.

Acknowledgments

The authors thank Professors Qing-Dong Cai, Chi-Wang Shu, Shu-Hai Zhang, Zhi-Jian Wang, and Tie Zhou for their valuable comments and suggestions. This work was supported in part by Ministry of Science and Technology of China, No. 2009CB724101, and Natural Science Foundation of China, Key Project No.10532010.

Appendix A. The formulae to compute the half-cell values in WIBS10

In WIBS10, from recordings on the neighboring cells $\{I_{i-2}, I_{i-1}, I_i, I_{i+1}, I_{i+2}, I_{i+3}\}$, $u^-_{i+1/2}$, $u^-_{i+1/2}$, $u^-_{i+1/6}$, $u^-_{i+1/3}$, $u^-_{i+2/3}$, and $u^-_{i+5/6}$ can be approximated to 10th order:

$$u^-_{i+1/6} = -\frac{3901783}{1062882000}v_{i-2,1} - \frac{6658423}{531441000}v_{i-2,2} - \frac{34247629}{1062882000}v_{i-1,1} - \frac{113339423}{531441000}v_{i-1,2} + \frac{1863223}{1574640}v_{i,1} + \frac{171662953}{59049000}v_{i,2} - \frac{149375321}{1062882000}v_{i+1,1} + \frac{357054577}{531441000}v_{i+1,2} - \frac{908599}{132860250}v_{i+2,1} + \frac{1503619}{66430125}v_{i+2,2},$$

$$u^-_{i+1/3} = \frac{20699154859}{4353564672000}v_{i-2,1} + \frac{34541024479}{2176782336000}v_{i-2,2} + \frac{174278385221}{2176782336000}v_{i-1,1} + \frac{221994016151}{544195584000}v_{i-1,2} + \frac{2872838579}{3224862720}v_{i,1} + \frac{272211312239}{60466176000}v_{i,2} + \frac{45668338429}{2176782336000}v_{i+1,1} - \frac{93508489849}{544195584000}v_{i+1,2} + \frac{14639988191}{4353564672000}v_{i+2,1} - \frac{24930464771}{2176782336000}v_{i+2,2},$$

$$u^-_{i+1/2} = \frac{29}{3000}v_{i-2,1} + \frac{49}{1500}v_{i-2,2} + \frac{377}{3000}v_{i-1,1} + \frac{1049}{1500}v_{i-1,2} + \frac{59}{120}v_{i,1} + \frac{6049}{1500}v_{i,2} + \frac{1073}{3000}v_{i+1,1} - \frac{817}{500}v_{i+1,2} + \frac{23}{1500}v_{i+2,1} - \frac{19}{375}v_{i+2,2},$$

$$u^-_{i+2/3} = \frac{30377191073}{4353564672000}v_{i-2,1} + \frac{51760387613}{2176782336000}v_{i-2,2} + \frac{165601161337}{2176782336000}v_{i-1,1} + \frac{122987791811}{272097792000}v_{i-1,2} + \frac{307729379}{3224862720}v_{i,1} + \frac{50947464479}{30233088000}v_{i,2} + \frac{1747203118313}{2176782336000}v_{i+1,1} - \frac{844600165189}{272097792000}v_{i+1,2} + \frac{82144259977}{4353564672000}v_{i+2,1} - \frac{133248465637}{2176782336000}v_{i+2,2},$$

$$u^-_{i+5/6} = -\frac{243347}{106288200}v_{i-2,1} - \frac{404597}{53144100}v_{i-2,2} - \frac{990479}{26572050}v_{i-1,1} - \frac{2570368}{13286025}v_{i-1,2} - \frac{18317}{98415}v_{i,1} - \frac{2030527}{1476225}v_{i,2} + \frac{16213087}{13286025}v_{i+1,1} - \frac{48925993}{13286025}v_{i+1,2} + \frac{571127}{106288200}v_{i+2,1} - \frac{843347}{53144100}v_{i+2,2}.$$

And $u^+_{i+1/2}$, $u^+_{i+1/6}$, $u^+_{i+1/3}$, $u^+_{i+2/3}$ and $u^+_{i+5/6}$ are a mirror symmetric of them with respect to $i + 1/2$:

$$u^+_{i+1/6} = -\frac{243347}{106288200}v_{i+3,1} + \frac{404597}{53144100}v_{i+3,2} - \frac{990479}{26572050}v_{i+2,1} + \frac{2570368}{13286025}v_{i+2,2} - \frac{18317}{98415}v_{i+1,1} + \frac{2030527}{1476225}v_{i+1,2} + \frac{16213087}{13286025}v_{i,1} + \frac{48925993}{13286025}v_{i,2} + \frac{571127}{106288200}v_{i-1,1} + \frac{843347}{53144100}v_{i-1,2},$$

$$u^+_{i+1/3} = \frac{30377191073}{4353564672000}v_{i+3,1} - \frac{51760387613}{2176782336000}v_{i+3,2} + \frac{165601161337}{2176782336000}v_{i+2,1} - \frac{122987791811}{272097792000}v_{i+2,2} + \frac{307729379}{3224862720}v_{i+1,1} - \frac{50947464479}{30233088000}v_{i+1,2} + \frac{1747203118313}{2176782336000}v_{i,1} + \frac{844600165189}{272097792000}v_{i,2} + \frac{82144259977}{4353564672000}v_{i-1,1} + \frac{133248465637}{2176782336000}v_{i-1,2},$$

$$u^+_{i+1/2} = \frac{29}{3000}v_{i+3,1} - \frac{49}{1500}v_{i+3,2} + \frac{377}{3000}v_{i+2,1} - \frac{1049}{1500}v_{i+2,2} + \frac{59}{120}v_{i+1,1} - \frac{6049}{1500}v_{i+1,2} + \frac{1073}{3000}v_{i,1} + \frac{817}{500}v_{i,2} + \frac{23}{1500}v_{i-1,1} + \frac{19}{375}v_{i-1,2},$$

$$u^+_{i+2/3} = \frac{20699154859}{4353564672000} v_{i+3,1} - \frac{34541024479}{2176782336000} v_{i+3,2} + \frac{174278385221}{2176782336000} v_{i+2,1} - \frac{221994016151}{544195584000} v_{i+2,2} + \frac{2872838579}{3224862720} v_{i+1,1} - \frac{272211312239}{60466176000} v_{i+1,2} + \frac{45668338429}{2176782336000} v_{i,1} + \frac{93508489849}{544195584000} v_{i,2} + \frac{14639988191}{4353564672000} v_{i-1,1} + \frac{24930464771}{2176782336000} v_{i-1,2},$$

$$u^+_{i+5/6} = -\frac{3901783}{1062882000} v_{i+3,1} + \frac{6658423}{531441000} v_{i+3,2} - \frac{34247629}{1062882000} v_{i+2,1} + \frac{113339423}{531441000} v_{i+2,2} + \frac{1863223}{1574640} v_{i+1,1} - \frac{171662953}{59049000} v_{i+1,2} - \frac{149375321}{1062882000} v_{i,1} - \frac{357054577}{531441000} v_{i,2} - \frac{908599}{132860250} v_{i-1,1} - \frac{1503619}{66430125} v_{i-1,2}.$$

References

[1] N.A. Adams, K. Shariff, A high-resolution hybrid compact-ENO scheme for shock–turbulence interaction problems, Journal of Computational Physics 127 (1996) 27–51.
[2] D.S. Balsara, C.-W. Shu, Monotonicity preserving weighted essentially non-oscillatory schemes with increasingly high order of accuracy, Journal of Computational Physics 160 (2000) 405–452.
[3] F. Bouchut, C. Bourdarias, B. Perthame, A MUSL method satisfying all the numerical entropy inequalities, Mathematics of Computation 65 (1996) 1439–1461.
[4] G. Capdeville, A Hermite upwind WENO scheme for solving hyperbolic conservation laws, Journal of Computational Physics 227 (2008) 2430–2454.
[5] B. Cockburn, C. Johnson, C.W. Shu, E. Tadmor, Essentially non-oscillatory and weighted essentially non-oscillatory schemes for hyperbolic conservation laws, in: A. quarteroni (Ed.), Advanced Numerical Approximation of Nonlinear Hyperbolic Equations, Lecture Notes in Mathematics, vol. 1697, Springer, Berlin, 1998, pp. 325–432.
[6] R.L. Dougherty, A.S. Edelman, J.M. Hyman, Nonnegativity-, monoticity-, or convexity preserving cubic quintic Hermite interpolation, Mathematics of Computation 52 (1989) 471–494.
[7] M. Dumbser, D. Balsara, E.F. Toro, C.D. Munz, A unified framework for the construction of one-step finite-volume and discontinuous Galerkin schemes, Journal of Computational Physics 227 (2008) 8209–8253.
[8] G. Jiang, C.W. Shu, Efficient implementation of weighted ENO schemes, Journal of Computational Physics 126 (1996) 202–228.
[9] L. Jiang, H. Shan, C.Q. Liu, Weighted compact scheme, International Journal of Computational Fluid Dynamics 15 (2001) 47–155.
[10] S.K. Lele, Compact finite difference schemes with spectral-like resolution, Journal of Computational Physics 103 (1992) 16–42.
[11] X. Liu, S. Osher, T. Chan, Weighted essentially non-oscillatory schemes, Journal of Computational Physics 115 (1994) 200–212.
[12] K. Mahesh, S.K. Lele, P. Moin, The influence of entropy fluctuations on the interaction of turbulence with a shock wave, Journal of Fluid Mechanics 334 (1997) 53–379.
[13] T. Nakamura, T. Tanaka, T. Yabe, K. Takizawa, Exactly conservative semi-Lagrangian scheme for multi-dimensional hyperbolic equations with directional splitting technique, Journal of Computational Physics 174 (2001) 171–207.
[14] S. Pirozzoli, Conservative hybrid compact-WENO schemes for schock-turbulence interaction, Journal of Computational Physics 178 (2002) 81–117.
[15] J. Qiu, C.-W. Shu, Hermite WENO schemes and their applications as limiters for Runge–Kutta discontinuous Galerkin method: one dimensional case, Journal of Computational Physics 193 (2004) 115–135.
[16] J. Qiu, C.-W. Shu. Hermite, WENO schemes and their applications as limiters for Runge–Kutta discontinuous Galerkin method: two dimensional case, Computers & Fluids 34 (2005) 642–663.
[17] C.W. Shu, S. Osher, Efficient implementation of essentially non-oscillatory shock-capturing schemes, Journal of Computational Physics 77 (1988) 439–471.
[18] C.W. Shu, S. Osher, Efficient implementation of essentially non-oscillatory shock capturing schemes II, Journal of Computational Physics 83 (1989) 261–268.
[19] B. Van-Leer, Towards the ultimate conservative difference scheme: III. A new approach to numerical convection, Journal of Computational Physics 23 (1977) 276–299.
[20] Z.J. Wang, High-order methods for the Euler and Navier–Stokes equations on unstructured grids, Progress in Aerospace Sciences 43 (2007) 1–41.
[21] S. Zhang, S. Jiang, C.-W. Shu, Development of nonlinear weighted compact schemes with increasingly higher order accuracy, Journal of Computational Physics 227 (2008) 7294–7321.
[22] E.F. Toro, Riemann Solvers and Numerical Methods for Fluid Dynamics, second ed., Springer Verlag, 1999.
[23] Dinshaw S. Balsara, Christoph Altmann, Claus-Dieter Munz, Michael Dumbser, A sub-cell based indicator for troubled zones in RKDG schemes and a novel class of hybrid RKDG + HWENO schemes, Journal of Computational Physics 226 (2007) 586C–620C.